energies

MDPI

Article

Review, Comparison, and Proposal for PWM Converters Integrating Differential Power Processing Converter for Small Exploration Rovers

Masatoshi Uno [1,*], Toshiki Shinohara [2], Yota Saito [1] and Akio Kukita [3]

1. College of Engineering, Ibaraki University, Hitachi 316-8511, Japan; yota.saito@murata.com
2. Toyota Motor Corporation, Toyota City 471-8571, Japan; toshiki_shinohara@mail.toyota.co.jp
3. Japan Aerospace Exploration Agency, Tsukuba 305-8505, Japan; kukita.akio@jaxa.jp

* Correspondence: masatoshi.uno.ee@vc.ibaraki.ac.jp

Received: 14 April 2019; Accepted: 16 May 2019; Published: 20 May 2019

check for updates

Abstract: Partial shading often appears on photovoltaic (PV) strings installed in small space probes, such as moon exploration rovers, due to their body structures, reducing the power yield of PV strings. Such partial shading issues can be precluded by differential power processing (DPP) converters. However, in addition to a main dc-dc converter, a DPP converter is required, increasing the system complexity and cost. In this paper, several kinds of integrated pulse width modulation (PWM) converters that can reduce the system complexity thanks to the integration are reviewed and are quantitatively compared in terms of the switch and magnetic component counts, and voltage conversion ratio. Based on the comparison and consideration from the perspectives of reliability, circuit volume, and voltage conversion requirement, a single-switch single-magnetic integrated PWM converter with a resonant voltage multiplier (RVM) was selected as the best suitable topology for small exploration rovers. Furthermore, the improved version with a non-resonant voltage multiplier (NRVM) was also proposed to achieve further circuit miniaturization and improved reliability. The experimental verification tests using the proposed integrated PWM converter were performed emulating a partial-shading condition. The maximum power yield from the PV modules was improved by 11.1% thanks to the DPP function of the proposed integrated converter.

Keywords: exploration rover; integrated converter; photovoltaic module; space probe; partial shading

1. Introduction

When a partial shading occurs on a photovoltaic (PV) string composed of multiple submodules (hereafter call modules for simplicity), module characteristics vary depending on the irradiance. Since shaded modules generate less current than do unshaded ones, a string current flows through a bypass diode connected in parallel with the shaded modules, as exemplified in Figure 1a, in which a PV string comprising two modules is illustrated. The power generation of the entire string significantly decreases because the shaded module no longer contributes to power generation due to the conduction of the bypass diode. Simulation analysis in past research showed that a partial shading equivalent to 10% of the area of a PV string installed on a residential roof leads to a 20%–30% decrease in the annual energy yield [1]. Furthermore, multiple maximum power points (MPPs), including one global MPP and local MPP(s), occur in *P-V* characteristics of partially-shaded strings (see Figure 1c), suggesting that ordinary MPP tracking (MPPT) algorithms may malfunction and the string works at a non-optimal point.

Partial shading is also a serious issue in space exploration rovers. A panning camera mounted on the top of an exploration rover often casts a shadow over PV panels, as shown in Figure 2. The decreased energy yield due to partial shading translates to the increased volume and mass of the

PV panel. Since the reduction in volume and mass is the top priority in spacecraft power systems, countermeasures for partial shading are an urgent demand in exploration rovers.

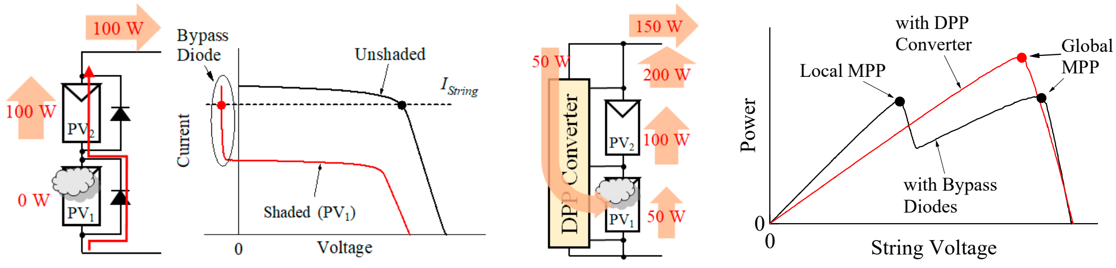

Figure 1. (**a**) Bypassed photovoltaic (PV) module due to partial shading, (**b**) power distribution in a differential power processing (DPP) converter, (**c**) string characteristics with bypass diode or DPP converter.

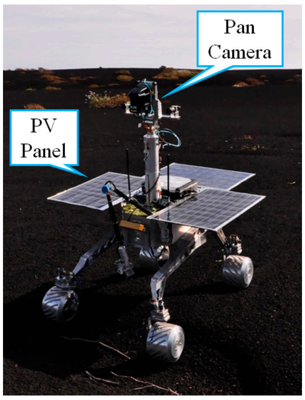

Figure 2. A photograph of the exploration rover.

Distributed MPPT systems [2], as well as various kinds of differential power processing (DPP) converters [3–24], have been proposed to tackle the partial shading issues. DPP converters are a converter that transfer power between adjacent modules or between a string and modules in order to eliminate the adverse effects of partial shading by virtually unifying electrical characteristics of all modules. An example of the power distribution by a DPP converter is depicted in Figure 1b. Suppose PV_1 and PV_2 are capable of generating 50 and 100 W, respectively, and the DPP converter is ideal with no loss. A fraction of the string power (50 W in this case) is redistributed to the shaded module of PV_1 via the DPP converter so that PV_1 behaves as if it can generate 100 W with the support of the DPP converter. In addition, since module characteristics are virtually unified by the power redistribution via the DPP converter, a local MPP vanishes and the power yield at the global MPP in the string's *P-V* characteristic dramatically increases, as depicted in Figure 1c. In summary, the DPP converter circulates 50 W, and an extractable maximum power is 150 W, significantly enhancing the power yield in comparison with the case of bypass diodes.

Despite the increased power yield under partial shading conditions, DPP converters are required in addition to the main dc-dc converter for string control, increasing the system complexity and cost. In this paper, conventional DPP converters and several kinds of integrated PWM converters that can reduce the system complexity thanks to the integration are reviewed and are quantitatively compared from various aspects. Based on the comparison, a suitable integrated converter topology is selected, and its improved version is also proposed. Finally, the efficacy of the proposed integrated PWM converter will be demonstrated based on the experimental verification tests.

2. Countermeasures for Partial Shading

2.1. Distributed MPPT System

A micro-converter, also known as a dc optimizer (see Figure 3a), is installed for each module to individually perform MPPT control and to extract maximum power from all modules [2]. This system tends to be complicated because it requires as many converters as modules. In addition, since each converter needs to be designed capable of the full power of the module, a larger power rating is required compared to DPP converters described later.

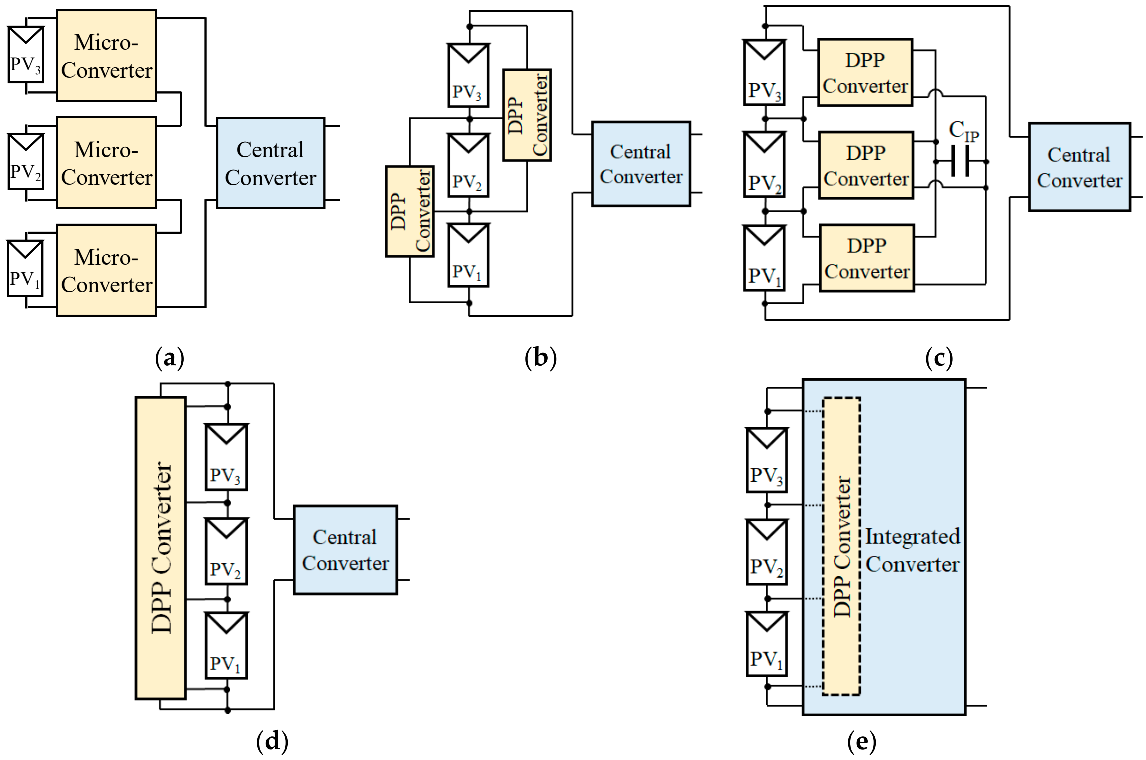

Figure 3. (**a**) Distributed MPPT system, (**b**) DPP converters for adjacent modules, (**c**) DPP converters with isolated port, (**d**) DPP converter between string and modules, (**e**) integrated converter.

2.2. DPP Converters for Adjacent Modules

DPP converters, which essentially are a bidirectional converter, transfer power between adjacent modules, as shown in Figure 3b, so that electrical characteristics of all modules are artificially unified even under partial shading conditions [3–15]. Since these DPP converters process only the power difference between adjacent modules, the power rating of the DPP converter can be rather smaller than that of micro-converters [3].

Figure 4 shows typical DPP converter topologies for adjacent modules. In addition to the need for not only a central converter but also multiple DPP converters in proportion to the number of modules, this system is prone to complexity because each DPP converter needs at least two switches for bidirectional power conversion—the switch count can be an indicator of circuit complexity because each switch requires an auxiliary circuit including a gate driver IC and its power supply. In addition, topologies in Figure 4a,b need multiple inductors in proportion to the number of modules, and therefore the circuit tends to be bulky and costly. Furthermore, each DPP converter transfers power only between adjacent modules, and the overall efficiency tends to decrease due to multiple power conversion stages as well as collective power conversion loss [15].

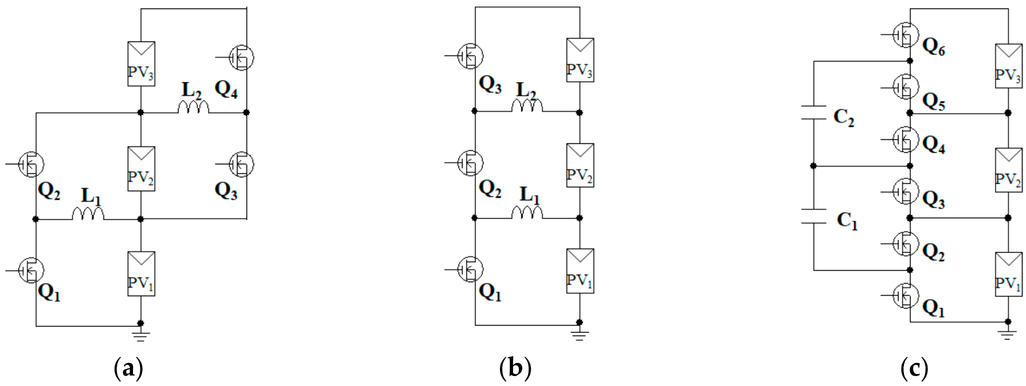

Figure 4. DPP converters for adjacent PV modules: (**a**) Bidirectional pulse width modulation (PWM) converter [3–8], (**b**) multistage chopper [9,10], (**c**) switched capacitor converter [11–14].

2.3. DPP Converters with Isolated Port

In the architecture using DPP converters with an isolated port (IP) of C_{IP} (see Figure 3c), bidirectional isolated converters, such as flyback converters, are generally employed [16–20]. Power transfer between not only adjacent modules but also remote modules is feasible via the IP, and therefore this architecture is advantageous for long PV strings consisting of numerous modules. However, since the number of DPP converters, each containing at least two switches and one isolation transformer, is equal to the module count, this architecture is prone to be more complex and costlier than the DPP architecture for adjacent modules.

2.4. DPP Converters between String and Modules

A DPP converter in this system transfers power directly from the string to shaded module(s) so that electrical characteristics of all modules are virtually unified to preclude partial shading issues [21–24]. Since one single DPP converter can handle multiple modules at a time, as shown in Figure 3d, the system can be simpler and less expensive than the aforementioned DPP architectures.

Figure 5 shows representative DPP converter topologies between string and modules. These DPP converters can be configured with a lower switch count when compared to the topologies shown in Figure 4, achieving a simplified circuit. However, in addition to the main converter for string power control, a DPP converter is still separately necessary. In other words, since two separate converters are required, there is room for improvement from the viewpoint of system simplification.

Topologies in Figure 5 have their own issues: the existence of a multi-winding transformer in Figure 4a is often a design hurdle [21], and the multi-stacked buck-boost converter in Figure 5b requires numerous inductors in proportion to the number of modules [22,23].

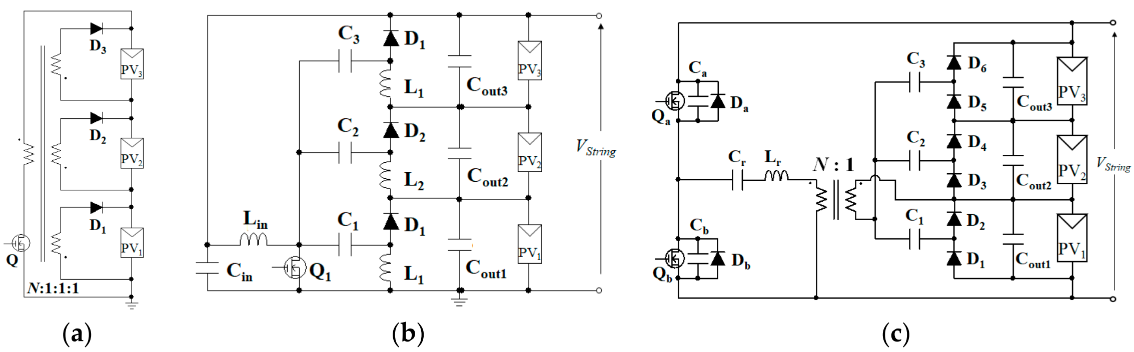

Figure 5. String-to-module DPP converters: (**a**) multi-winding flyback converter [21], (**b**) multi-stacked buck-boost converter [22,23], (**c**) series resonant voltage multiplier [24].

2.5. Integrated Converters

The integrated converter architecture in Figure 3e, which can be derived from sharing circuit parts between two converters, performs both the DPP function and string control [25–28]. The numbers of circuit parts, as well as converters, can be reduced by the integration, realizing the system simplification, cost reduction, and enhanced reliability. However, since two functions of DPP converter and string power control are integrated into a single unit, performance optimization is no longer feasible. Therefore, energy yield from a PV string tends to be smaller in comparison to the systems using the main converter and DPP converters separately (Figure 3b–d).

3. Requirements for Power System in Small Exploration Rovers

From the viewpoint of electrical performance requirement, there are no significant differences between spacecraft and terrestrial applications. However, given the requirements for power systems in small spacecraft, there are four major aspects that significantly influence selections of electric parts, circuit topologies, and system architectures. In the following, these aspects are discussed and considered.

(1) Simplest possible control circuit due to poor product line-up of rad-hard electrical parts: Radiation-tolerant (or rad-hard) electric parts must be used in converters in spacecraft, and therefore, careful consideration for parts selection and circuit design is mandatory. Specifically, poor product line-up of rad-hard electric parts, especially ICs and micro-controllers, greatly limits the parts selection and circuit design. In terrestrial applications, for example, various kinds of dedicated low-cost ICs and micro-controllers are readily available in the market, and converters relying on complex control techniques can be relatively easily implemented thanks to the low-cost high-performance electric parts. In spacecraft applications, on the other hand, rad-hard ICs and micro-controllers are extremely expensive (e.g., a rad-hard micro-controller costs a few ten thousand dollars) or even unavailable, and hence, control circuits must be often configured using discrete electric parts. Therefore, converters in spacecraft desirably operate with the simplest possible control circuit, and ultimately, a control circuit should be omitted. In other words, converters operable with an open-loop control is an ideal choice.

(2) Reliability improvement by minimizing electric parts count: Since components in the spacecraft cannot be repaired nor replaced after launching, the reliability is always of great importance. The reduction in the electric parts count is the key to improving the reliability, and the reduction of semiconductor switches, which have a complicated structure compared to passive elements, is particularly effective. Furthermore, as described in Section 2.2, since an auxiliary circuit is required to drive each switch, converters that can operate with a few switches will greatly contribute to improving the reliability.

(3) Reduction in volume and mass from circuit viewpoint: Given that the reduction in volume and mass is the top priority in spacecraft electrical systems, bulky circuit parts, such as magnetic components and film capacitors, are desirably eliminated from converters.

(4) Reduction in volume and mass from system architecture viewpoint: In the conventional medium- to large-scale spacecraft of several hundred watt to several kilo-watt classes, PV panels occupy a large portion of a total mass in spacecraft power systems. To reduce the total mass, spacecraft power systems are designed such that the energy yield from PV panels is maximized. In other words, a power system having a main dc-dc converter and DPP converter separately (Figure 3b–d) would be a desirable power system architecture for medium- to large-scale spacecraft—the main dc-dc converter and DPP converter can be individually optimized in the architecture in Figure 3b–d. In small-scale spacecraft, on the other hand, the relative mass of PV panels is not significant, and the reduction in the number of components is the most effective approach to achieve the total mass reduction. Therefore, integrated converters that can reduce the number of components is advantageous in small spacecraft applications.

The next subsection focuses only on integrated converters to select a topology suitable for small exploration rovers.

4. Integrated PWM Converters

As discussed in the previous section, integrated converters are suitable for small exploration rovers from the viewpoint of the reduction in volume and mass of the system. Meanwhile, converters operable with an open-loop control are ideal from the viewpoint of the rad-hard electric parts selection. This section introduces integrated PWM converter topologies that do not need feedback control for DPP functions. In other words, all the integrated converter topologies in this section meet the requirement regarding (1) and (4) discussed in Section 3.

Figure 6a–e shows the five integrated PWM converter topologies for two PV modules connected in series. All topologies can perform both the DPP function and string power control at a time, but each topology has unique advantages and drawbacks depending on the foundation circuit.

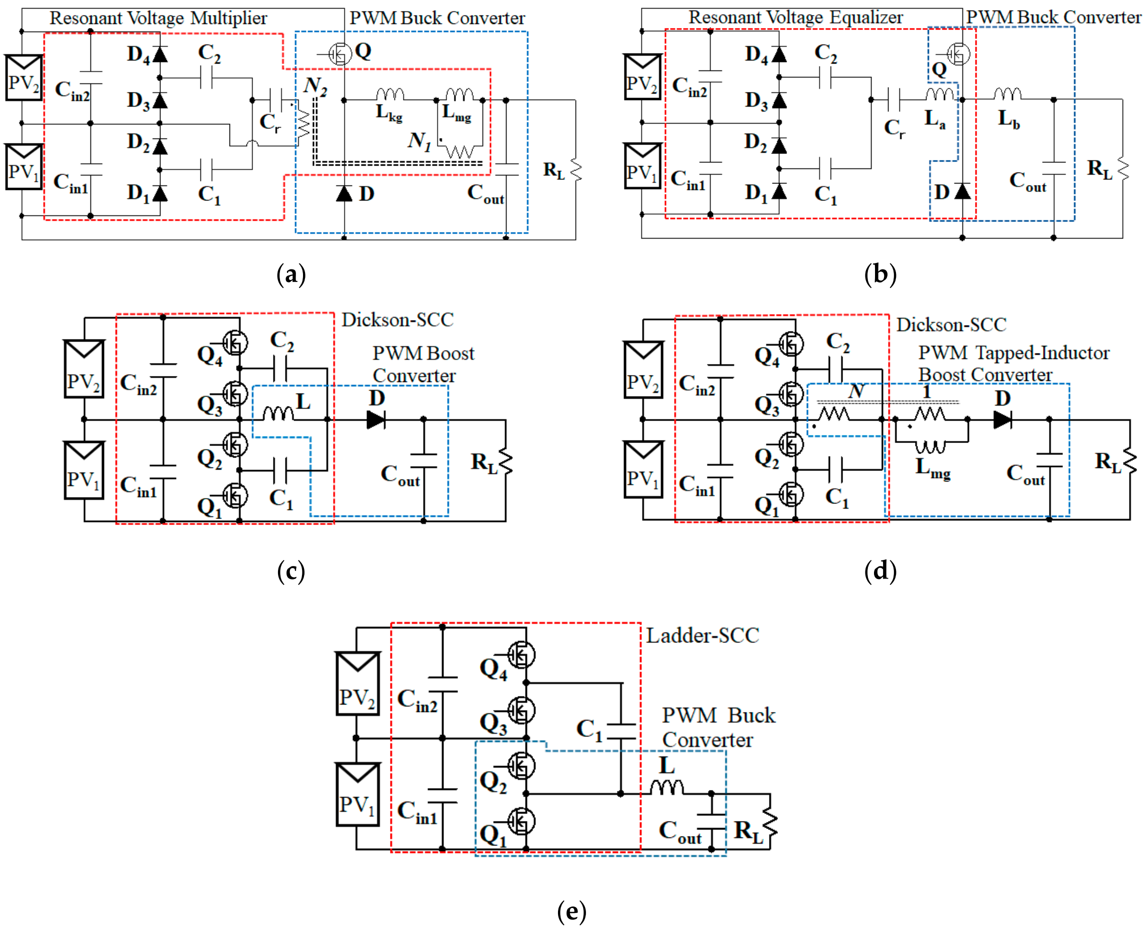

Figure 6. Integrated PWM converters: (**a**) Single-switch single-magnetic converter integrating resonant voltage multiplier (RVM), (**b**) Single-switch transformer-less converter, (**c**) Dickson-SCC converter, (**d**) Dickson-SCC tapped-inductor converter, (**e**) Ladder-SCC buck converter.

4.1. Single-Switch Single-Magnetic PWM Converter with Resonant Voltage Multiplier

This topology is derived based on the combination of a resonant voltage multiplier (RVM) [25,26] and a PWM buck converter, as shown in Figure 6a. The magnetizing inductance L_{mg} of the transformer acts as a filter inductor of the PWM buck converter. The square wave voltage generated across the secondary winding drives the RVM circuit that plays a role of the DPP converter. The single-switch single-magnetic topology realizes a simple and compact circuit.

When the voltage of a PV module decreases due to partial shading, power from the string is automatically redistributed to the shaded module via the RVM. In other words, no control is needed for DPP function, and controlling only the PWM buck converter automatically realizes DPP function [25,26].

4.2. Single-Switch Transformerless PWM Converter with Resonant Voltage Multiplier

Similar to the topology in Section 4.1, the RVM is driven by the square wave voltage generated in the PWM buck converter. Since two inductors are required (Figure 6b), this integrated converter would be bulkier than the single-switch single-magnetic integrated converter introduced in the previous subsection.

The RVM in this integrated converter always operates regardless of the occurrence of partial shading. Since the operation of the RVM causes unnecessary losses under unshaded conditions, this integrated converter is considered suitable for small spin satellites where partial shading always occurs.

4.3. Dickson-SCC-Based PWM Converter

This topology (Figure 6c) is derived from the combination of a Dickson switched capacitor converter (SCC) and a PWM boost converter [28]. The negative influences of partial shading are precluded by the Dickson SCC that equalizes module voltages automatically. Odd- and even-numbered switches are alternately driven so that power is transferred between adjacent modules [11]. A large number of switches are necessary, and therefore the circuit is prone to complexity in comparison to the single-switch topologies, likely reducing the reliability due to the increased number of circuit parts. On the other hand, there is only one inductor and its stored energy is partly shared by capacitors, and hence the inductor can be significantly downsized [29,30].

This SCC-based topology allows significant circuit miniaturization compared with the single-switch topologies and thus is suitable for micro- and nano-satellites that prioritize system miniaturization rather than the reliability.

4.4. Dickson-SCC-Based Tapped-Inductor PWM Converter

This is an extended version of the Dickson-SCC-based converter discussed in Section 4.3. A tapped-inductor is introduced as an extra design freedom to adjust a voltage conversion ratio, as shown in Figure 6d.

4.5. Ladder-SCC-Based PWM Buck Converter

The ladder-SCC-based integrated PWM buck converter, shown in Figure 6e, is the combination of a ladder-SCC and a PWM buck converter [27]. Similar to the Dickson-SCC-based topologies, the circuit miniaturization is feasible thanks to capacitors. In comparison with the Dickson-SCC-based topologies in Figure 6c,d, the capacitor count can be slightly reduced, achieving a simpler and less expensive circuit.

5. Comparison and Selection of Integrated Converter for Small Exploration Rovers

In the integrated converters with the RVM or SCC introduced in Section 4, controlling the PWM converter only automatically realizes the DPP function. In other words, both the RVM and SCC circuits can perform the DPP function with open-loop control and, therefore, are suitable for spacecraft power systems as these topologies meet the requirement regarding (1) and (4) discussed in Section 3. Hence, in the following, integrated converter topologies are compared from the viewpoint of the reliability and volume (i.e., the points of (2) and (3) in Section 3).

As mentioned in Section 2.2, the switch count is an indicator of circuit complexity, and converters with fewer switches are a desirable topology from the viewpoint of the reliability. Meanwhile, since the magnetic components are the bulkiest circuit element in converters, the magnetic component count can be regarded as an indicator of the circuit volume and mass. Needless to say, converters must meet the requirement of voltage conversion ratios necessary in specific applications. With these aspects taken into consideration, the quantitative comparison is made from the viewpoints of the switch count, magnetic component count, and voltage conversion ratio (V_{load}/V_{string}).

Table 1 compares the five kinds of integrated PWM converters introduced in Section 4. V_{string} is an input voltage, V_{load} is a load voltage, and d is a duty cycle of switches. N is the turn ratio of the tapped-inductor.

Table 1. Quantitative comparison for integrated PWM converters.

Topology	Switch Count	Magnetic Component Count	Voltage Conversion Ratio
Single-Switch Single-Magnetic	1	1	d
Single-Switch Transformerless	1	2	d
Dickson-SCC	4	1	$\frac{1+d}{2}$
Dickson-SCC Tapped-Inductor	4	1	$\frac{1}{2}\left(1+\frac{1+N}{N}d\right)$
Ladder-SCC	4	1	$\frac{d}{2}$

The electrical requirement in small exploration rovers is described below. A PV panel consists of two modules connected in series, and its voltage V_{string} is 16 V (V_{PV} = 8.0 V). Two lithium-ion battery cells connected in series are directly connected to the load, and V_{load} varies in the range of 6.0–8.4 V. From the given values of V_{string} and V_{load}, the required voltage conversion ratio is 0.375–0.525.

Figure 7 shows and compares the voltage conversion ratios of the five integrated PWM converters as a function of the duty cycle. Two types of single-switch integrated converters (i.e., the single-switch single-magnetic converter and single-switch transformer-less converter) meet the voltage conversion requirement in the entire range, whereas voltage conversion ratios of SCC-based integrated converters are out of the required range. Based on the pairwise comparison between the two single-switch integrated PWM converters, the single-switch single-magnetic topology is advantageous in terms of the magnetic component count. In addition, partial shading does not always occur in exploration rovers, unlike the spin satellites where some portion of PV panels is always shaded, the single-switch single-magnetic integrated converter is also advantageous in terms of power conversion efficiency under unshaded conditions—in the single-switch transformerless topology, currents unnecessarily flow toward substrings even under unshaded conditions, generating unnecessary losses. The above comparison and discussion conclude that the single-switch single-magnetic integrated PWM converter is the best suitable topology for small exploration rovers.

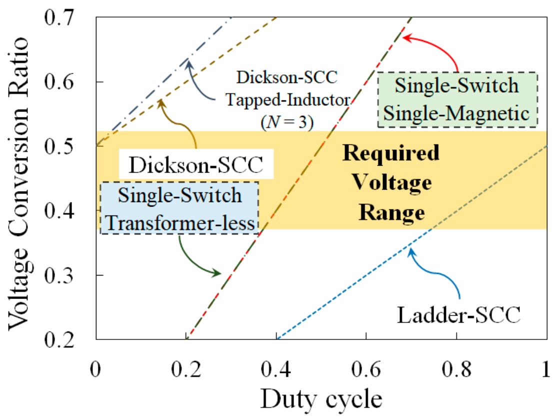

Figure 7. Voltage conversion ratios of five integrated PWM converters.

6. Operation Analysis for Single-Switch Single-Magnetic Integrated PWM Converter with Non-Resonant Voltage Multiplier

6.1. Circuit Description and Its Features

The conventional single-switch single-magnetic integrated PWM converter with the RVM requires a resonant capacitor C_r for its resonant operation, as shown in Figure 6a. In general, a film capacitor is used for C_r because its capacitance must be accurate and independent on a bias voltage. However, as discussed in Section 3, film capacitors are relatively bulky and are desirably omitted from circuits to achieve reduced circuit volume and mass. In this paper, we propose an integrated PWM converter with a non-resonant voltage multiplier (NRVM), as shown in Figure 8, where C_r is eliminated to further simplify and miniaturize the circuit and to further improve the reliability. The proposed topology is a non-isolated dc-dc converter that can also be applied to standalone PV systems, not only to space applications.

In the conventional integrated PWM converter with the RVM (see Figure 6a), the current in the RMV is a discontinuous sinusoidal wave, and hence, Joule losses tend to be large due to relatively large peak currents. In the proposed integrated PWM converter with the NRVM, on the other hand, the current in the NRVM is a continuous triangular wave (see Figure 9), and the current continuity helps reduce the peak currents and Joule losses, compared to the conventional RVM. Current waveforms of the NRVM and RVM will be compared in Section 6.3.

Unlike the conventional RVM, characteristics of the NRVM are dependent on the duty cycle of the switch Q. In other words, the DPP function of the NRVM varies with the duty cycle, and the characteristics of the NRVM need to be modeled in order to accurately estimate behaviors of a PV panel supported by the NRVM under partial shading conditions. In the next section, the mathematical model of the NRVM will be derived based on the detailed operation analysis.

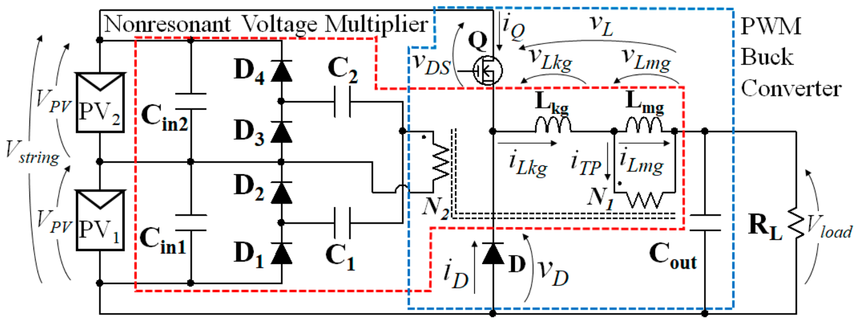

Figure 8. Proposed single-switch single-magnetic PWM converter integrating non-resonant voltage multiplier (NRVM).

6.2. Operation Analysis

The operation analysis is performed for a representative case that PV_1 is partially shaded. Key operation waveforms and current flow paths are shown in Figures 9 and 10, respectively. T_s in Figure 9 is the switching period. The fundamental operating principle is identical to that of an ordinary PWM buck converter. The analysis in this section is performed based on the premise that all circuit parts are ideal, and a time constant τ formed by L_{kg} and C_1 or C_2 is far longer than the switching period so that i_{Lkg} is assumed to change linearly.

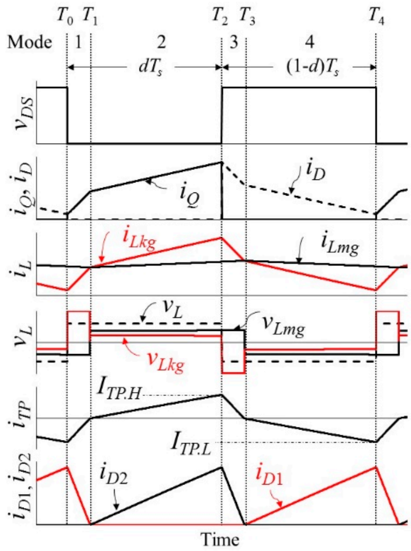

Figure 9. Key operation waveforms when PV_1 is partially shaded.

Mode 1 ($T_0 < t \leq T_1$) (Figure 10a): The voltage across the primary winding of the transformer v_L is equal to $V_{string} - V_{load}$. In the NRVM, the current of C_1, i_{C1}, flows through the low-side diode D_1. The current flowing through the primary winding i_{TP} corresponds to the difference between the current of the leakage inductance i_{Lkg} and the current of the magnetizing inductance i_{Lmg}. Since the primary winding current can be obtained from the voltages of L_{kg} and L_{mg}, v_{Lkg} and v_{Lmg}, respectively, i_{TP} in Mode 1 can be expressed as

$$i_{TP.1}(t) = \left\{\frac{1-d}{L_{kg}} V_{string} + \left(\frac{1}{L_{kg}} + \frac{1}{L_{mg}}\right)\frac{N_1}{N_2}(V_{PV} - V_{C1})\right\} t - I_{TP.L} \tag{1}$$

where V_{C1}, d, and $I_{TP.L}$ are the average voltage of C_1, the duty cycle of Q, and the initial current of i_{TP} in Mode 1, respectively.

Mode 2 ($T_1 < t \leq T_2$) (Figure 10b): Q is still on, so v_L is the same as that in Mode 1. The high-side diode D_2 starts conducting on the transformer secondary side. Meanwhile, v_{Lkg} and v_{Lmg} change as the direction of i_{C1} is reversed on the secondary side. i_{TP} in Mode 2 is expressed as

$$i_{TP.2}(t) = \left\{\frac{1-d}{L_{kg}} V_{string} - \left(\frac{1}{L_{kg}} + \frac{1}{L_{mg}}\right)\frac{N_1}{N_2} V_{C1}\right\} t \tag{2}$$

Mode 3 ($T_2 < t \leq T_3$) (Figure 10c): Q is turned off and $v_L = -V_{out}$, but D_2 is still conducting. The polarity of v_{Lkg} is reversed as the current flow path on the primary side changes. i_{TP} in Mode 3 is given by

$$i_{TP.3}(t) = -\left\{\frac{d}{L_{kg}} V_{string} + \left(\frac{1}{L_{kg}} + \frac{1}{L_{mg}}\right)\frac{N_1}{N_2} V_{C1}\right\} t + I_{TP.H} \tag{3}$$

where $I_{TP.H}$ is the initial current of i_{TP} in Mode 3, as designated in Figure 8.

Mode 4 ($T_3 < t \leq T_4$) (Figure 10d): D_1 begins to conduct again. The polarities of both the v_{Lkg} and v_{Lmg} change as the current flow path on the secondary side changes. i_{TP} in Mode 4 is expressed as

$$i_{TP.4}(t) = -\left\{\frac{d}{L_{kg}} V_{string} - \left(\frac{1}{L_{kg}} + \frac{1}{L_{mg}}\right)\frac{N_1}{N_2}(V_{PV} - V_{C1})\right\} t. \tag{4}$$

Based on Equations (2) and (4), $I_{TP.L}$ and $I_{TP.H}$ in Equations (1) and (3) can be yielded as

$$\begin{cases} I_{TP.H} = \left\{\frac{1-d}{L_{kg}}V_{string} - \left(\frac{1}{L_{kg}} + \frac{1}{L_{mg}}\right)\frac{N_1}{N_2}V_{C1}\right\}(dT_S - t_d) \\ I_{TP.L} = -\left\{\frac{d}{L_{kg}}V_{string} - \left(\frac{1}{L_{kg}} + \frac{1}{L_{mg}}\right)\frac{N_1}{N_2}(V_{PV} - V_{C1})\right\}\left\{(1-d)T_S - \frac{1-d}{d}t_d\right\} \end{cases} \tag{5}$$

where t_d is a length of Mode 1, and $((1-d)/d)t_d$ corresponds to the period of Mode 3. This is derived from the relationship of d: $t_d = (1-d)$: T_{32}, assuming the period of Mode 3 to be T_{32} [31].

$$t_d = \frac{-\frac{T_s}{2V_{PV}}\left(\frac{d}{2d-1}\right)^2\left\{(2d-1)(V_{LA}-V_{PV}) + \frac{(2d-1)(1-d)}{d}V_{PV} - V_{LA}\right\}}{-\sqrt{\left\{(2d-1)(V_{LA}-V_{PV}) + \frac{(2d-1)(1-d)}{d}V_{PV} - V_{LA}\right\}^2 - 4\frac{(2d-1)^2}{d}(1-d)(V_{LA}-V_{PV})}} \tag{6}$$

$$V_{LA} = \frac{N_2}{N_1}\frac{L_{mg}}{L_{kg}+L_{mg}}V_{in}.$$

The current of C_1 in each mode is given by the following equation using the transformer turns ratio and i_{TP}, as

$$i_{Ci(m)}(t) = \frac{N_1}{N_2}i_{TP(m)}(t) \tag{7}$$

where the subscript number $m = 1 \ldots 4$ is the mode number. As the average voltage of the transformer winding must be zero, the average voltage of C_1, V_{C1}, is given by

$$V_{C1} = V_{PV1}\left(1 - d + \frac{t_d}{T_S} - \frac{1-d}{d}\frac{t_d}{T_S}\right). \tag{8}$$

Since the average current of C_1 under steady-state conditions is zero, the current supplied to the shaded module, I_{VM}, is equal to the average current of D_1 and D_2. Therefore, I_{VM} can be expressed as

$$I_{VM} = \frac{1}{2T_S}\int_0^{T_S}|i_{C1}|dt = \frac{N_1}{N_2}\frac{(1-d)\left(dT_S - \frac{2d-1}{d}t_d\right)(dT_S - t_d)}{2T_S L_{kg}}\Delta V \tag{9}$$

where ΔV is given by

$$\Delta V = V_{string} - \frac{N_1}{N_2}\frac{1}{1-d}\frac{L_{kg}+L_{mg}}{L_{mg}}V_{C1}. \tag{10}$$

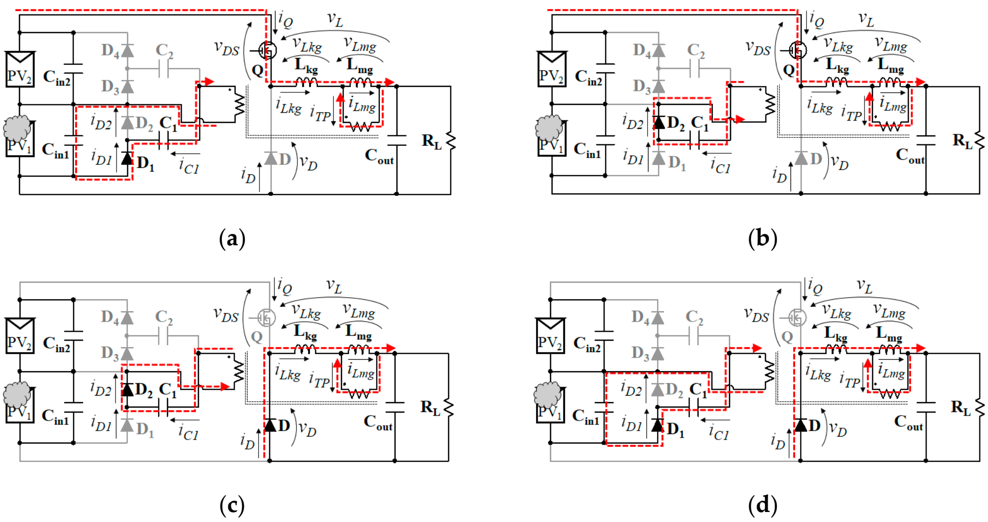

Figure 10. Current flow paths in (**a**) Mode 1, (**b**) Mode 2, (**c**) Mode 3, and (**d**) Mode 4.

6.3. Waveform Comparison between NRVM and Conventional RVM

Current waveforms of i_{TP} in the proposed NRVM and conventional RVM are compared in Figure 11—i_{TP} is taken for the comparison because it represents all currents in the voltage multiplier. i_{TP} in the conventional RVM is a discontinuous sinusoidal wave and its peak value $I_{peak.RVM}$ tends to be large due to the discontinuity. On the other hand, i_{TP} in the NRVM is a continuous triangular wave and its peak value $I_{peak.NRVM}$ can be smaller than $I_{peak.RVM}$. The reduced peak current in the proposed NRVM reduces Joule losses in the voltage multiplier, eventually resulting in increased power yield from the PV panel. The increased power yield by the NRVM will be experimentally demonstrated in Section 7.3.

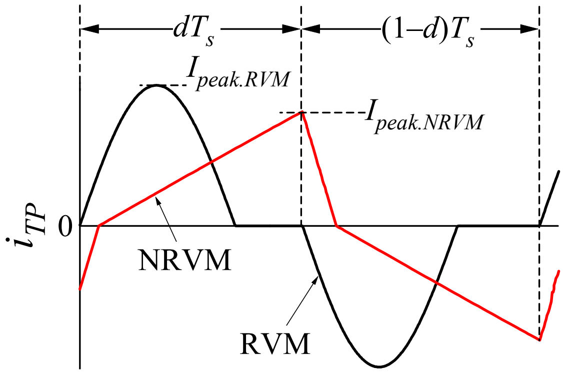

Figure 11. Waveform comparison between NRVM and RVM.

6.4. DC Equivalent Circuit

In the past work, the dc equivalent circuit of the single-switch single-magnetic integrated PWM converter with the RVM has been derived [25], as shown in Figure 12. The ideal transformer with the turn ratio of 1:d represents the PWM buck converter. The circuit consisting of the ideal multi-winding transformer, diodes, and equivalent resistors (R_{eq1} and R_{eq2}) corresponds to the RVM. In this section, the equivalent resistance in the dc equivalent circuit of the NRVM is derived.

Equation (10) represents the voltage relationship on the primary winding of the ideal multi-winding transformer. ΔV is the voltage drop across the equivalent resistance $R_{eq.p}$, and the second term on the right-hand side is the reflected voltage across the primary winding. Based on Equations (7), (9), and (10), the average absolute value of i_{TP}, I_{TP}, can be obtained. Assuming ΔV as the voltage drop due to the equivalent resistance, the following equation is yielded

$$I_{TP} = \frac{N_2}{N_1} I_{VM} = \frac{(1-d)\left(dT_S - \frac{2d-1}{d} t_d\right)(dT_S - t_d)}{2T_S L_{kg}} \Delta V = \frac{1}{R_{eq.p}} \Delta V. \tag{11}$$

From Equation (11), the equivalent resistance $R_{eq.p}$ existing on the primary side of the ideal multi-winding transformer is given by

$$R_{eq.p} = \frac{2T_S L_{kg}}{(1-d)\left(dT_S - \frac{2d-1}{d} t_d\right)(dT_S - t_d)}. \tag{12}$$

Next, to derive the equivalent resistance R_{eq1} of the NRVM, the voltage variation of C_1 is considered based on [32]. Let $V_{C1.D1}$ be the voltage of C_1 in Modes 1 and 4, during which D_1 conducts. Similarly, $V_{C1.D2}$ is the voltage of C_1 when D_2 conducts in Modes 2 and 3. $V_{C1.D1}$ and $V_{C1.D2}$ can be expressed as

$$\begin{cases} V_{C1.D1} = V_{s.p} + V_f - rI_{VM} \\ V_{C1.D2} = -V_{s.n} - V_f + rI_{VM} \end{cases} \tag{13}$$

where $V_{s.p}$ and $V_{s.n}$ are the secondary winding voltage in each mode, r is the total resistance of the current path in the NRVM, and V_f is the forward voltage drop of a diode. The voltage variation of C_1, ΔV_{C1}, is given by

$$\Delta V_{C1} = V_{C1.D1} - V_{C1.D2} = \left(V_{s.p} + V_{s.n}\right) + 2\left(V_f - rI_{VM}\right) - V_{PV}. \tag{14}$$

Since I_{VM} is a current rectified by the NRVM,

$$\Delta V_{C1} = \frac{I_{VM}}{C_1 f_s}. \tag{15}$$

From Equations (14) and (15),

$$V_{s.p} + V_{s.n} = V_s = \frac{I_{VM}}{C_1 f_s} + V_{PV} + 2\left(V_f - rI_{VM}\right). \tag{16}$$

Rearrangement of Equation (16) produces

$$V_s - V_{PV} = \left(2r + \frac{1}{C_1 f_s}\right)I_{VM} - 2V_f = R_{eq1}I_{VM} - 2V_f. \tag{17}$$

From Equation (17), the equivalent resistance R_{eq1} is obtained as

$$R_{eq1} = 2r + \frac{1}{C_1 f_s}. \tag{18}$$

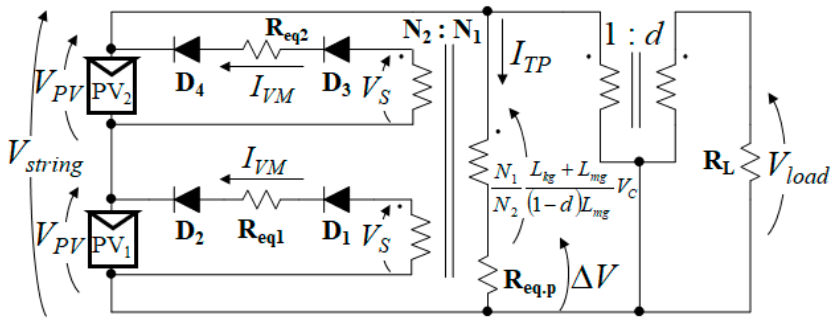

Figure 12. DC Equivalent circuit.

6.5. *Operation Conditions of NRVM*

The output voltage of the NRVM is equal to the peak-to-peak value of the voltage applied to the secondary winding, and the voltage applied to each module is ideally $(N_2/N_1)V_{string}$ [25]. If $(N_2/N_1)V_{string}$ is lower than the module voltage V_{PV}, the NRVM is inactive. Therefore, considering the forward voltage drop of diodes V_f, the transformer turn ratio needs to satisfy the following equation

$$\frac{N_2}{N_1} \geq \frac{V_{PV} + 2V_f}{V_{string}}. \tag{19}$$

7. Experimental Results

7.1. *Prototype*

A 30-W prototype of the proposed integrated PWM converter with the NRVM for two modules connected in series was built, as shown in Figure 13. Table 2 shows the circuit parts used for the prototype. The switching frequency was 100 kHz. For the sake of experimental convenience, a MOSFET was used instead of the free-wheeling diode D, and the prototype was operated in a synchronous mode. The power conversion efficiency at the full load of 30 W under an unshaded condition was measured to be as high as 93%.

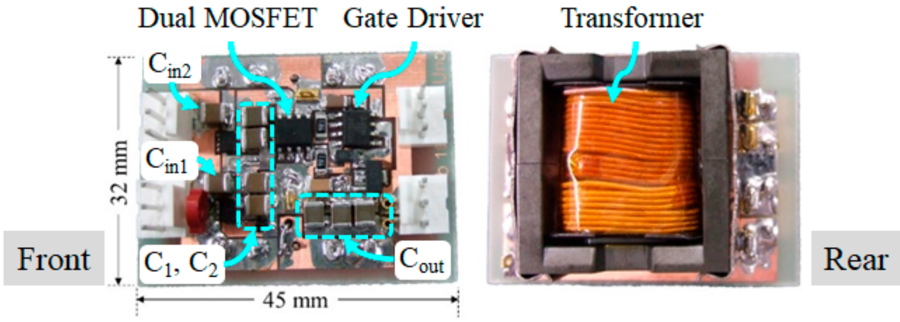

Figure 13. 30-W prototype.

Table 2. Circuit parts used for the prototype.

Component	Value
C_1, C_2	Ceramic Capacitor, 30 µF, 16 V
C_{in1}, C_{in2}	Ceramic Capacitor, 50 µF, 16 V
D_1–D_4	Dual Schottky Barrier Diode, SBE813, V_f = 0.435 V
Q_1, Q_2	Dual MOSFET, IRF7341, R_{on} = 50 mΩ
C_{out}	Ceramic Capacitor, 66 µF
Transformer	N_1:N_2 = 8:4, L_{mg} = 32 µH, L_{kg} = 0.94 µH EFD 30 Core (N87), 30-Strand Litz Wire with Diameter of 0.66 mm

7.2. Output Characteristics of NRVM

The characteristics of the NRVM were measured using the experimental setup shown in Figure 14a. An external power supply V_{in} of 16 V was used, instead of PV modules. A variable resistor R_{var} was connected in parallel with C_{in1} to simulate the current flow paths under the PV_1-shaded condition. V_{Cin1} and I_{Rvar} were measured while changing R_{var}. The load resistance R_L was adjusted so that I_{load} was 0 or 2.8 A. i_{Lkg} and i_{C1} were measured using a current probe (TCP312A, Tektronix, Portland, OR, USA)—Litz wires were inserted in series with the transformer's primary winding and C_1 in order to measure the currents. To verify the derived model in Section 6, the output characteristics of the NRVM were calculated based on the dc equivalent circuit shown in Figure 14b. Conditions and circuit parameters were identical to those of the experiment, while r in (18) was set to be 140 mΩ based on the experimentally-measured resistance.

The measured and calculated characteristics are shown and compared in Figure 15. The experimental results satisfactorily matched with the calculations, verifying the mathematical model derived in Section 6. V_{Cin1} linearly decreased as I_{Rvar} increased. I_{Rvar} was nearly 0 A in the region where V_{Cin1} was higher than 7.3 V. From the provided values in Table 2 (N_2/N_1 = 0.5 and V_f = 0.435 V), this result verified that I_{Rvar} flowed only in the range where Equation (19) was satisfied. V_{Cin1} with d = 30% and 70% decreased steeper than that with d = 50% due to the increased equivalent resistance $R_{eq.p}$—Equation (12) implies that $R_{eq.p}$ increases as d moves away from 50%. On the other hand, the measured characteristics were nearly independent on I_{load}, suggesting that the characteristics of the NRVM were not influenced by load currents.

Measured key waveforms at V_{load} = 8.0 V and I_{load} = 2.8 A are shown in Figure 16. The measured current waveforms were slightly blunt, not completely linear, because of a time constant τ of L/R formed by L_{kg} and resistive components of the diode and secondary winding. Although slightly different from the theoretical waveforms in Figure 9, the measured waveforms showed a good agreement, verifying the operation of the prototype.

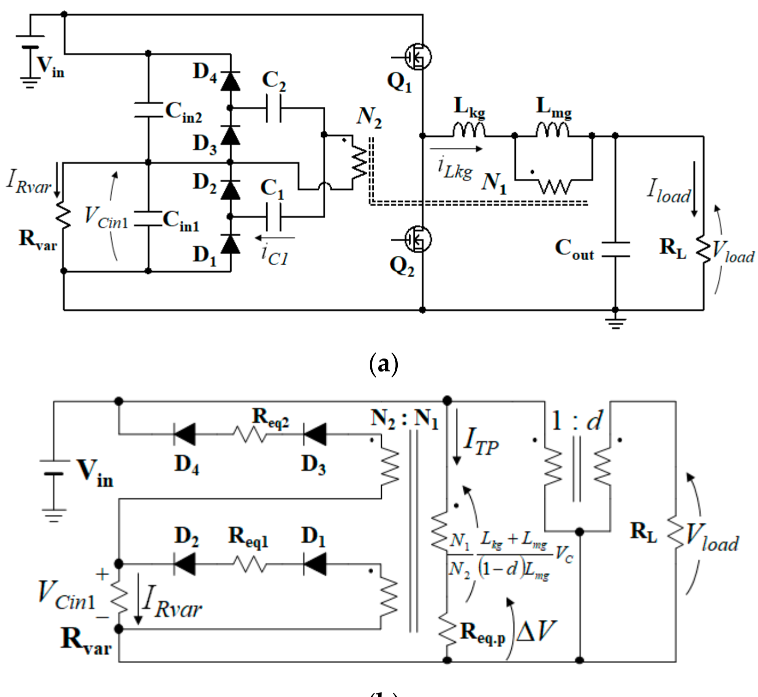

Figure 14. (**a**) Experimental and (**b**) dc equivalent circuit set up to measure output characteristic of NRVM.

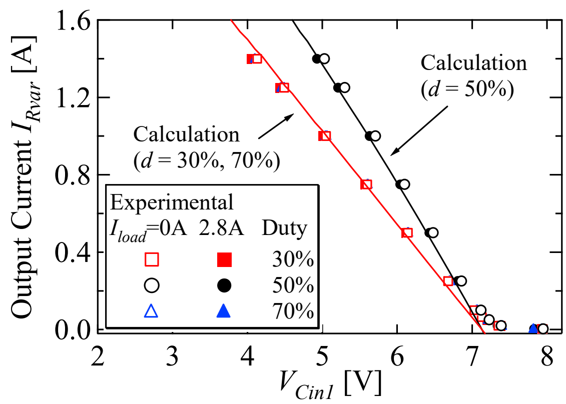

Figure 15. Measured and calculated output characteristic of NRVM.

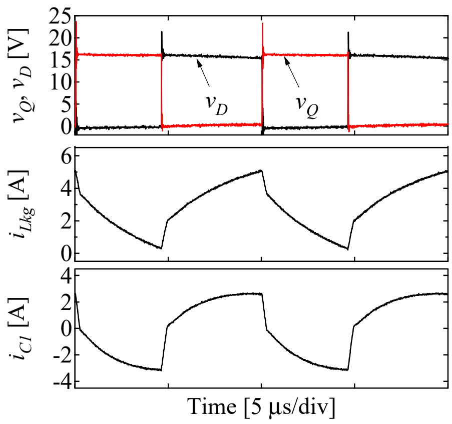

Figure 16. Measured key operation waveforms at V_{load} = 8.0 V and I_{load} = 2.8 A.

7.3. Experiments Emulating Partial Shading Condition

String characteristics with/without the prototype were measured under a partial shading condition. Solar array simulators (E4361A, Keysight Technologies, Santa Rosa, CA, USA) were used to emulate a partial shading condition. The electrical characteristics of the modules used in the experiment are shown in Figure 17a. The short-circuit current of PV_1 was set to be half of PV_2, assuming the case that PV_1 was severely shaded. String characteristics were measured under three cases: (1) with the proposed integrated converter with the NRVM, (2) with the conventional integrated converter with the RVM, (3) without the integrated converter (i.e., with traditional bypass diodes).

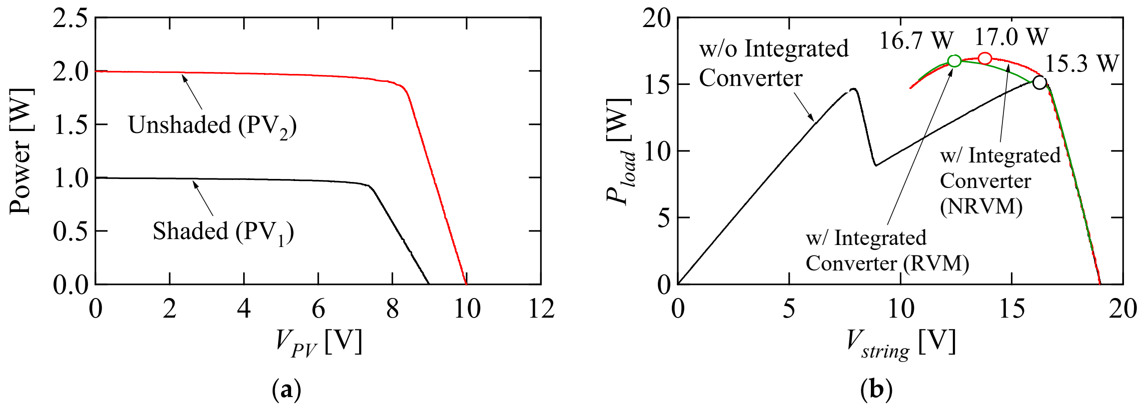

Figure 17. Experimental results: (**a**) Individual module characteristics, (**b**) measured string characteristics with/without integrated PWM converter.

As for case (1), a constant voltage load of 8.0 V was used as R_L, and d was manually varied in the range of $d \leq 0.8$ in order to sweep the string characteristics. For case (2), in order to compare the performances of the proposed NRVM and conventional RVM, the prototype was retrofitted to be the conventional integrated converter with the RVM by inserting a resonant capacitor C_r (ECWU1105KCV, 1 μF × 3 parallel) in series with the secondary winding. The resonant frequency was 182 kHz. The conditions of d and the load voltage in case (2) were identical to those in case (1). In case (3), the integrated converter was removed, and the string characteristic was swept between zero and the open-circuit voltage by directly connecting an electronic load to the string.

The measured string characteristics are shown and compared in Figure 17b. Without the integrated converter, there were two MPPs observed in the measured P–V characteristic, and the maximum power at the global MPP was merely 15.3 W at V_{string} = 16.2 V. In this case, the shaded module PV_1 was bypassed and did not contribute to power generation, similar to the case shown in Figure 1a. Meanwhile, with the integrated converters, V_{string} was swept in the range between 10.5 V and the open-circuit voltage of 19 V, corresponding to the duty cycle variation of $d \leq 0.8$. In the region of $V_{string} > 16.5$ V, in which Equation (19) was not satisfied, the NRVM did not operate, and therefore, the measured P_{load} characteristics were independent on whether the integrated converter was used. In the region of $V_{string} < 16.5$ V, on the other hand, P_{load} was significantly improved by the integrated converter because a fraction of the string power was redistributed to the shaded module of PV_1—this power redistribution scenario is identical to the case discussed in Section 6.2. With the integrated converter with the NRVM, the maximum power increased to as high as 17.0 W at V_{string} = 13.7 V, corresponding to 11.1% improvement in the power yield. Meanwhile, the measured maximum power with the conventional RVM was 16.7 W at V_{string} = 12.4 V, corresponding to a 9.2% improvement. The slightly-inferior power yield of 1.9 points was attributable to the increased Joule loss due to the relatively large peak resonant current, as compared in Figure 11.

In summary, with the integrated converter, the local MPP successfully vanished, and the power yield drastically increased. These results demonstrated the superior performance of the proposed integrated PWM converter with the NRVM.

7.4. Verification for DC Equivalent Circuit

A simulation-based test using the dc equivalent circuit was also performed emulating the partial shading condition identical to that of the experiment. PV module characteristics were emulated by look-up tables. $R_{eq.p}$ in the equivalent circuit was programmed to obey Equation (12).

The string characteristics with/without the dc equivalent circuit of the integrated converter (see Figure 12) are shown in Figure 18. The simulation results slightly differed from the experimental characteristics shown in Figure 17b probably because resistive components were ignored to simplify the analysis and the derivation of the dc equivalent circuit. However, the simulation and experimental results satisfactorily matched, indicating the validity of the derived dc equivalent circuit.

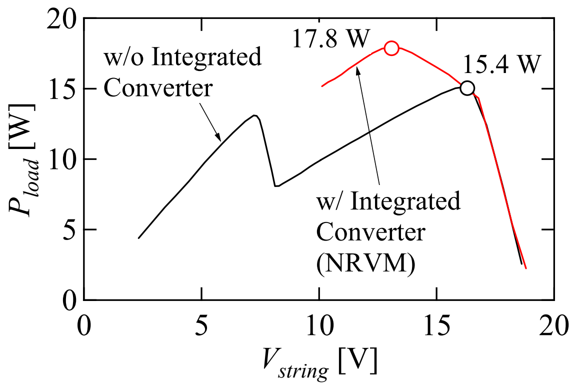

Figure 18. DC equivalent circuit-based simulation results.

8. Conclusions

PV strings in small exploration rovers suffer from partial shading issues because of a panning camera mounted on the top of the exploration rovers. Solutions to the partial shading issues, including conventional DPP architectures and topologies, were reviewed from various aspects, such as electrical parts count and circuit volume. Integrated DPP converters, which can reduce the component count by the integration, are an attractive architecture in small exploration rovers where the reduction in the number of components is the most effective approach to achieve the total mass reduction. Hence, integrated DPP converters only were focused on the following review and comparison.

Several types of PWM converters integrating DPP converters were reviewed, and the quantitative comparison was made for the switch count, the magnetic component count, and the voltage conversion ratio, with considering the requirements of power systems in small exploration rovers. The single-switch single magnetic integrated PWM converter with the RVM was selected as the best suitable topology because of its circuit simplicity and less magnetic component count.

The improved integrated PWM converter with the NRVM that eliminates a bulky film capacitor was also proposed to achieve further circuit miniaturization and improved reliability. Furthermore, the reduced peak current thanks to the non-resonant operations of the NRVM achieves improved power conversion efficiency. The detailed operation analysis was performed to derive the mathematical model, followed by the derivation of the dc equivalent circuit.

The experimental verification tests using the 30-W prototype of the integrated PWM converter with the NRVM or the conventional RVM were performed emulating the partial shading condition. In comparison with the case of traditional bypass diodes, the integrated converters with the NRVM and RVM improved the power yield by 11.1% and 9.2%, respectively, demonstrating its efficacy. The slightly-superior power yield of 1.9 points was attributable to the reduced Joule loss thanks to the lower peak currents by the non-resonant operations of the NRVM. The experimental results satisfactorily matched with the simulation results of the derived dc equivalent circuit, verifying the mathematical model obtained from the operation analysis.

Author Contributions: Conceptualization, M.U.; methodology, M.U. and T.S.; simulation analysis, T.S. and Y.S.; validation, T.S. and Y.S.; writing—original draft preparation, M.U. and T.S.; writing—review and editing, M.U.; supervision, M.U. and A.K.

Funding: This research received no external funding.

Conflicts of Interest: The authors declare no conflict of interest.

References

1. MacAlpine, S.M.; Erikson, R.W.; Brandemuehl, M.J. Characterization of power optimizer potential to increase energy capture in photovoltaic systems operating under nonuniform conditions. *IEEE Trans. Power Electron.* **2013**, *28*, 2936–2945. [CrossRef]
2. Vitelli, M. On the necessity of joint adoption of both distributed maximum power point tracking and central maximum power point tracking in PV systems. *Prog. Photovolt. Res. Appl.* **2014**, *22*, 283–299. [CrossRef]
3. Kim, K.A.; Shenoy, P.S.; Krein, P.T. Converter rating analysis for photovoltaic differential power processing systems. *IEEE Trans. Ind. Electron.* **2015**, *30*, 1987–1997. [CrossRef]
4. Shenoy, P.S.; Kim, K.A.; Johnson, B.B.; Krein, P.T. Differential power processing for increased energy production and reliability of photovoltaic systems. *IEEE Trans. Ind. Power Electron.* **2013**, *28*, 2968–2979. [CrossRef]
5. Bergveld, H.J.; Büthker, D.; Castello, C.; Doorn, T.; Jong, A.D.; Otten, R.V.; Waal, K.D. Module-level dc/dc conversion for photovoltaic systems: The delta-conversion concept. *IEEE Trans. Power Electron.* **2013**, *28*, 2005–2013. [CrossRef]
6. Zaman, M.S.; Wen, Y.; Fernandes, R.; Buter, B.; Doorn, T.; Dijkstra, M.; Bergveld, H.J.; Trescases, O. A cell-level differential power processing IC for concentrating-PV systems with bidirectional hysteretic current-mode control and closed-loop frequency regulation. *IEEE Trans. Power Electron.* **2015**, *30*, 7230–7244. [CrossRef]
7. Qin, S.; Cady, S.T.; García, A.D.D.; Podgurski, R.C.N.P. A distributed approach to maximum power point tracking for photovoltaic submodule differential power processing. *IEEE Trans. Power Electron.* **2015**, *30*, 2024–2040. [CrossRef]
8. Qin, S.; Barth, C.B.; Podgurski, R.C.N.P. Enhancing microinverter energy capture with submodule differential power processing. *IEEE Trans. Power Electron.* **2016**, *31*, 3575–3585. [CrossRef]
9. Shimizu, T.; Hashimoto, O.; Kimura, G. A novel high-performance utility-interactive photovoltaic inverter system. *IEEE Trans. Power Electron.* **2003**, *18*, 704–711. [CrossRef]
10. Shimizu, T.; Hirakata, M.; Kamezawa, T.; Watanabe, H. Generation control circuit for photovoltaic modules. *IEEE Trans. Power Electron.* **2001**, *16*, 293–300. [CrossRef]
11. Stauth, J.T.; Seeman, M.D.; Kesarwani, K. Resonant switched-capacitor converters for sub-module distributed photovoltaic power management. *IEEE Trans. Power Electron.* **2013**, *28*, 1189–1198. [CrossRef]
12. Chang, A.H.; Avestruz, A.T.; Leeb, S.B. Capacitor-less photovoltaic cell-level power balancing using diffusion charge redistribution. *IEEE Trans. Power Electron.* **2015**, *30*, 537–546. [CrossRef]
13. Blumenfeld, A.; Cervera, A.; Peretz, M.M. Enhanced differential power processor for PV systems: Resonant switched-capacitor gyrator converter with local MPPT. *IEEE J. Emerg. Sel. Top. Power Electron.* **2014**, *2*, 883–892. [CrossRef]
14. Uno, M.; Saito, Y.; Yamamoto, M.; Urabe, S. PWM switched capacitor-based cell-level power balancing converter utilizing diffusion capacitance of photovoltaic cells. *IEEE Trans. Power Electron.* **2019**, in press. [CrossRef]
15. Poshtkouhi, S.; Biswas, A.; Trescases, O. Dc-dc converter for high granularity, sub-string MPPT in photovoltaic applications using a virtual-parallel connection. In Proceedings of the 27th Annual IEEE Applied Power Electronics Conference and Exposition (APEC), Orlando, FL, USA, 5–9 February 2012; pp. 86–92.
16. Olalla, C.; Clement, D.; Rodríguez, M.; Makisimović, D. Architectures and control of submodule integrated dc-dc converters for photovoltaic applications. *IEEE Trans. Power Electron.* **2013**, *28*, 2980–2997. [CrossRef]
17. Olalla, C.; Deline, C.; Clement, D.; Levron, Y.; Rodríguez, M.; Makisimović, D. Performance of power limited differential power processing architectures in mismatched PV systems. *IEEE Trans. Power Electron.* **2015**, *30*, 618–631. [CrossRef]

18. Bell, R.; Podgurski, R.C.N.P. Decoupled and distributed maximum power point tracking of series-connected photovoltaic submodules using differential power processing. *IEEE J. Emerg. Sel. Top. Power Electron.* **2015**, *3*, 881–891. [CrossRef]
19. Levron, Y.; Clement, D.R.; Choi, B.; Olalla, C.; Maksimovic, D. Control of submodule integrated converters in the isolated-port differential power-processing photovoltaic architecture. *IEEE J. Emerg. Sel. Top. Power Electron.* **2014**, *2*, 821–832. [CrossRef]
20. Chu, G.; Wen, H.; Jiang, L.; Hu, Y.; Li, X. Bidirectional flyback based isolated-port submodule differential power processing optimizer for photovoltaic applications. *Sol. Energy* **2017**, *158*, 929–940. [CrossRef]
21. Du, J.; Xu, R.; Chen, X.; Li, Y.; Wu, J. A novel solar panel optimizer with self-compensation for partial shadow condition. In Proceedings of the 28th Annual IEEE Applied Power Electronics Conference and Exposition (APEC), Long Beach, CA, USA, 17–21 March 2013; pp. 92–96.
22. Uno, M.; Kukita, A. Single-switch voltage equalizer using multi-stacked buck-boost converters for partially-shaded photovoltaic modules. *IEEE Trans. Power Electron.* **2015**, *30*, 3091–3105. [CrossRef]
23. Uno, M.; Kukita, A. Current sensorless equalization strategy for a single-switch voltage equalizer using multistacked buck–boost converters for photovoltaic modules under partial shading. *IEEE Trans. Ind. Electron.* **2017**, *53*, 420–429. [CrossRef]
24. Uno, M.; Kukita, A. Two-switch voltage equalizer using an LLC resonant inverter and voltage multiplier for partially-shaded series-connected photovoltaic modules. *IEEE Trans. Ind. Appl.* **2015**, *51*, 1587–1601. [CrossRef]
25. Uno, M.; Kukita, A. Single-switch single-magnetic PWM converter integrating voltage equalizer for partially-shaded photovoltaic modules in standalone applications. *IEEE Trans. Power Electron.* **2018**, *33*, 1259–1270. [CrossRef]
26. Uno, M.; Shinohara, T. Variable switching frequency modulation scheme for PWM converter integrating series-resonant voltage multiplier-based voltage equalizer for photovoltaic strings under partial shading. *IEEJ Trans. Electr. Eng.* **2019**, *14*, 467–474. [CrossRef]
27. Uno, M.; Kukita, A. PWM converter integrating switched capacitor converter and series-resonant voltage multiplier as equalizers for photovoltaic modules and series-connected energy storage cells for exploration rovers. *IEEE Trans. Power Electron.* **2017**, *32*, 8500–8513. [CrossRef]
28. Uno, M.; Yamamoto, M. Switched Capacitor-Based PWM Converter Integrating String Converter and Voltage Equalizer for Photovoltaic Strings under Partial Shading. In Proceedings of the IEEE Region Ten Conference (TENCON), Penang, Malaysia, 5–8 November 2017; pp. 1058–1063.
29. Sanders, S.R.; Alon, E.; Le, H.P.; Seeman, M.D.; Jhon, M.; Ng, V.W. The road to fully integrated DC-DC conversion via the switched-capacitor approach. *IEEE Trans. Power Electron.* **2013**, *28*, 4146–4155. [CrossRef]
30. Uno, M.; Kukita, A. PWM switched capacitor converter with switched-capacitor-inductor cell for adjustable high step-down voltage conversion. *IEEE Trans. Power Electron.* **2019**, *34*, 425–437. [CrossRef]
31. Yashiro, K.; Uno, M. Transformer-less bidirectional PWM converter integrating voltage multiplier-based cell voltage equalizer for series-connected electric double-layer capacitors. *IEEE Trans. Power Electron.* **2019**, *34*, 4304–4315. [CrossRef]
32. Uno, M.; Kukita, A. Bidirectional PWM converter integrating cell voltage equalizer using series-resonant voltage multiplier for series-connected energy storage cell. *IEEE Trans. Power Electron.* **2015**, *30*, 3017–3090. [CrossRef]